

MITIGATING SHEAR-DEPENDENT OBJECT DETECTION BIASES WITH METACALIBRATION

ERIN S. SHELDON,¹ MATTHEW R. BECKER,² NIALL MACCRANN,^{3,4} AND MICHAEL JARVIS⁵

¹ Brookhaven National Laboratory, Bldg 510, Upton, New York 11973, USA

² High Energy Physics Division, Argonne National Laboratory, Lemont, IL 60439, USA

³ Center for Cosmology and Astro-Particle Physics, The Ohio State University, Columbus, OH 43210, USA

⁴ Department of Physics, The Ohio State University, Columbus, OH 43210, USA

⁵ Department of Physics and Astronomy, University of Pennsylvania, Philadelphia, PA 19104, USA
Draft version August 18, 2020

ABSTRACT

METACALIBRATION is a new technique for measuring weak gravitational lensing shear that is unbiased for isolated galaxy images. In this work we test METACALIBRATION with overlapping, or “blended” galaxy images. Using standard METACALIBRATION, we find a few percent shear measurement bias for galaxy densities relevant for current surveys, and that this bias increases with increasing galaxy number density. We show that this bias is not due to blending itself, but rather to shear-dependent object detection. If object detection is shear independent, no deblending of images is needed, in principle. We demonstrate that detection biases are accurately removed when including object detection in the METACALIBRATION process, a technique we call METADETECTION. This process involves applying an artificial shear to images of small regions of sky and performing detection on the sheared images, as well as measurements that are used to calculate a shear response. We demonstrate that the method can accurately recover weak shear signals even in highly blended scenes. In the METACALIBRATION process, the space between objects is sheared coherently, which does not perfectly match the real universe in which some, but not all, galaxy images are sheared coherently. We find that even for the worst case scenario, in which the space between objects is completely unsheared, the resulting shear bias is at most a few tenths of a percent for future surveys. We discuss additional technical challenges that must be met in order to implement METADETECTION for real surveys.

1. INTRODUCTION

Recently developed methods to estimate weak gravitational lensing shear can in principle provide calibration at the 0.1% level or better, sufficient for the requirements of future weak lensing surveys (e.g., [Huterer et al. 2006](#)). At the time of writing, two methods have demonstrated sufficient accuracy without reliance on calibration from simulations, including rigorous mathematical formalisms to deal with selection effects: the BFD method ([Bernstein et al. 2016](#)) and the METACALIBRATION method ([Huff & Mandelbaum 2017](#); [Sheldon & Huff 2017](#)). The FPFs method of [Li et al. \(2018\)](#) is also able to achieve the required accuracy using an iterative method to deal with selection effects. However, these methods do not deal explicitly with an important aspect of the real universe: the images of objects overlap on the sky and thus the light from separate objects is “blended” (for discussion of blending effects see, e.g., [Dawson et al. 2016](#)).

METACALIBRATION can, in principle, be used to calibrate any shear-dependent measurement biases, even those associated with blending. However, we will show below that there is a particular calibration bias associated with the process of detecting objects in the presence of blending, and this is not addressed in naive implementations of METACALIBRATION. This bias, if left unaddressed, will greatly exceed the strict requirements for future lensing surveys ([Huterer et al. 2006](#)), in which blending will be prevalent ([Dawson et al. 2016](#)).

At this stage it is worthwhile to define exactly what we mean by object detection. For isolated objects, object detection is closely related to the identification of regions of an image with pixel values above some threshold. But when objects overlap on the sky, whether due to physical association or chance projection, it may be useful to

determine how many objects there are in each detected region. This may be important, for example, when calculating a redshift distribution for a set of detections. We associate this process of identifying the individual objects in a super-threshold region with detection. We reserve the term “deblending” to specifically mean the process of assigning a fraction of the light in each pixel to each detected object, which may or may not be a feature of the object detection. In this work, for the sake of brevity, we will use the terms “detection” and “object detection” interchangeably.

In the weak shear regime, the lensing mapping is one-to-one and preserves surface brightness ([Schneider et al. 1992](#)). For such a mapping, object detection need not be shear dependent. For example, an object detection algorithm that finds connected regions in an image with pixel values above a threshold will not in principle be shear dependent. This is because the topology of the contours, or the number of closed contours, at a given surface brightness will not change under a shear, due to the preservation of surface brightness and the one-to-one nature of the mapping. However, in real observations the image resolution is degraded by a point-spread-function (PSF) due to the atmosphere, telescope optics and detector. In this case the overlap of objects, and also the topology of contours of a given surface brightness, does depend on shear because the PSF convolution occurs after the shear mapping. This effect is demonstrated in [Figure 1](#). Thus the simple threshold object detection method described above will manifest a shear-dependent object detection bias. Note this effect is present even in the absence of pixel noise, so blended objects well above the detection threshold will also manifest a detection bias.

Common object detection schemes in use today, such

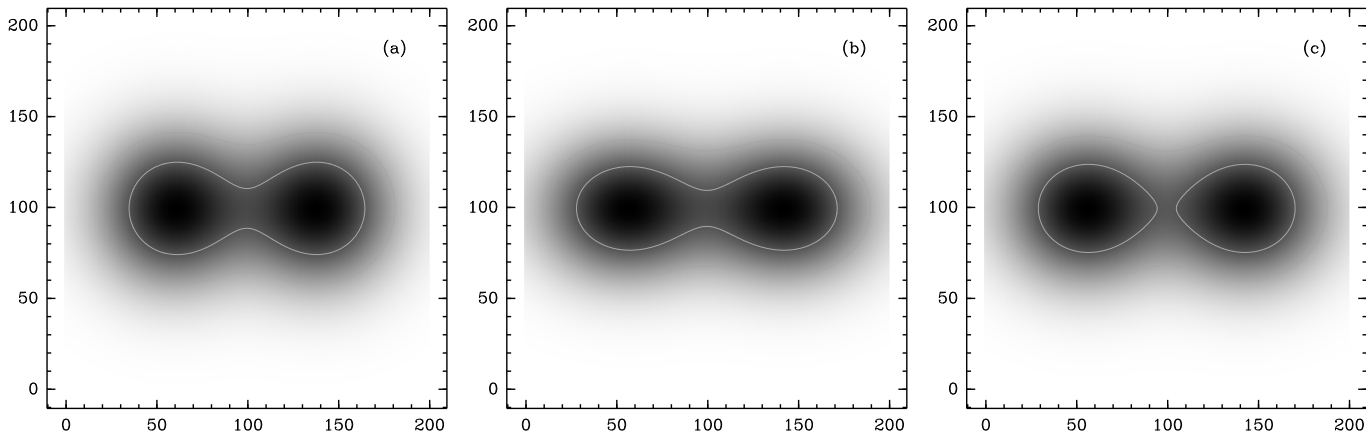


Figure 1. Toy example of shear-dependent object detection in the presence of a PSF. In panel (a) two objects are present, convolved by a PSF with no shear. Contours represent constant brightness. In panel (b) the objects are sheared by $\gamma = (0.0, 0.1)$ after the PSF convolution. The contour levels are the same as panel (a). In this case the inner contours for the two objects overlap before and after application of the shear. This is a general property of the shear transformation in the weak regime: surface brightness is preserved under shear, and because the mapping is one-to-one, the topology is also preserved. In panel (c) the shear is applied before the PSF convolution, which mimics real sky images. In this case the inner contours do not overlap after shearing, and two objects may be detected rather than one. For case (c) an object detection algorithm that identified connected regions above a threshold as a single object would manifest a shear-dependent object detection bias.

at those in SOURCE EXTRACTOR (Bertin & Arnouts 1996) and the pipelines used for the Hyper-Surprime Camera survey and the Rubin Observatory Legacy Survey of Space and Time (LSST) (Bosch et al. 2018a,b) are based on thresholding, similar to the simple approach described above but differing in complexity and efficiency. The detection and splitting procedure is demonstrated clearly for SOURCE EXTRACTOR in Bertin & Arnouts (1996) Figure 2. As we will show, the object detections produced by SOURCE EXTRACTOR do manifest shear dependence. Even a simple local peak finder, run on a smoothed image, has similar properties and manifests the bias. An open question, which we will not address in this work, is whether it is possible to derive a shear-independent object detection algorithm in the presence of a PSF and a detector with finite spatial resolution. Such an algorithm would in principle eliminate the shear-dependent object detection biases explored in this work.

Published implementations of METACALIBRATION (e.g., Huff & Mandelbaum 2017; Sheldon & Huff 2017), when used with the common object detection schemes discussed above, are expected to exhibit shear-dependent object detection biases. These implementations of METACALIBRATION work by applying artificial shears to small “postage stamp” images. These postage stamps are extracted from a larger image at the locations of objects found during an *independent* object detection step, run before the application of METACALIBRATION. Measurements on the sheared images are then used to calculate a linear response of an ellipticity measurement to the applied shear. Because the independent object detection already manifests a shear-dependent object detection bias, the shear applied when running METACALIBRATION does not properly reflect the full response to shear.

Object detection effects can be naturally incorporated into METACALIBRATION by shearing larger images, rather than small postage stamps, and re-running the object detection algorithm on each of the sheared images. We call this technique METADETECTION to indicate that detection is part of the METACALIBRATION process. An rough

outline of the method is as follows:

1. Artificially shear images of small regions of sky.
2. Perform detection and measurement on the sheared images, as well as images without artificial shear. Due to shear-dependent detection effects, the number of detections found the each image will be slightly different, resulting in different object catalogs.
3. Calculate ensemble shear statistics using measurements from the unsheared images.
4. Use measurements from sheared images to calculate a linear response of the measurements to a shear.
5. Correct the ensemble shear statistics using the response.

The ensemble mean ellipticities are taken over different catalogs, whereas in Sheldon & Huff (2017) all measurements were performed using a single static detection catalog.

As we will demonstrate, METADETECTION can correct for biases associated with shear-dependent detection, in addition to model bias, pixel noise bias and ordinary shear-dependent selection effects.

An alternative route being explored by the community is to calibrate shear measurements using simulations (see, e.g., Fenech Conti et al. 2017; Mandelbaum et al. 2018). The idea is to use an uncalibrated ellipticity measurement, which can manifest a large shear bias (of order 10%) and unknown selection and detection effects. The final shear measurements are then calibrated using a simulation that matches the data as closely as possible. Ultimately METADETECTION may have some remaining biases that must be calibrated with simulations. Our goal in developing this algorithm is to make these biases as small as possible, sub-percent as opposed to 10 percent,

which we expect will greatly reduce the sensitivity of the final calibration to small inaccuracies in the simulation.

The paper is laid out as follows. In Section 2 we introduce a generalized METACALIBRATION that accounts for shear dependent object detection. In Section 3, we describe the simulations we use to test our methods and the analysis techniques used to infer the shear signal. In Section 4, we study the effects of object detection on shear measurements with METACALIBRATION. In Section 5, we describe in detail our implementation of METADETECTION and apply it to recover the shear signal in our simulations. We also discuss the physical limits of METADETECTION. In Section 6, we study the effects of the PSF variation on METADETECTION. Finally, we conclude in Section 8.

2. METACALIBRATION AND METADETECTION

In this section we introduce an extension of METACALIBRATION that naturally accounts for shear-dependent object detection.

METACALIBRATION is a general technique that computes the linear response of measurements on an image to an applied shear using only the observed image. For a small applied shear γ , we can expand a two-component measurement \mathbf{e} as

$$\begin{aligned} \mathbf{e} &\approx \mathbf{e}|_{\gamma=0} + \left. \frac{\partial \mathbf{e}}{\partial \gamma} \right|_{\gamma=0} \gamma + O(\gamma^2) \\ &\equiv \mathbf{e}|_{\gamma=0} + \mathbf{R}\gamma + O(\gamma^2) \end{aligned} \quad (1)$$

where \mathbf{R} is the response matrix of the image measurement at zero applied shear, $R_{ij} = \partial e_i / \partial \gamma_j$, with i and j taking all combinations of the two shear components. The measurement \mathbf{e} can be, for example, an ellipticity measurement, and in what follows we will use the term ellipticity without loss of generality.

We estimate the response using a numerical, finite-difference derivative

$$R_{ij} \approx \frac{e_i^+ - e_i^-}{\Delta \gamma_j}. \quad (2)$$

where R_{ij} is the estimated response of the measurement to shear and $\Delta \gamma_j = 2\gamma_j$ is the difference between two applied shears, $\pm \gamma_j$, with γ_j a small shear of order 0.01.

The quantity $e_i^{+/-}$ is the i -th ellipticity component measured on an image sheared with $\pm \Delta \gamma_j$. The creation of artificially sheared images requires careful handling of the PSF and other observational effects (Sheldon & Huff 2017).

Because the estimated responses are noisy for a single object, we average the response over many images and objects.

Let's examine the case of estimating the mean shear from a mean ellipticity. In Sheldon & Huff (2017) we wrote the mean ellipticity as

$$\langle \mathbf{e} \rangle \approx \left\langle \left. \frac{\partial \mathbf{e}}{\partial \gamma} \right|_{\gamma=0} \gamma \right\rangle = \langle \mathbf{R}\gamma \rangle \quad (3)$$

The mean shear was then estimated using the mean re-

sponse:

$$\begin{aligned} \langle \mathbf{R} \rangle &= \left\langle \left. \frac{\partial \mathbf{e}}{\partial \gamma} \right|_{\gamma=0} \right\rangle, \\ \langle R_{ij} \rangle &= \left\langle \frac{e_i^+ - e_i^-}{\Delta \gamma_j} \right\rangle, \\ \langle \gamma \rangle &\approx \langle \mathbf{R} \rangle^{-1} \langle \mathbf{e} \rangle. \end{aligned} \quad (4)$$

Note that the derivative appears *inside* the averages, implying we could take the derivative for each object separately. This is possible for a single static catalog: postage stamp images are generated for each object, artificially sheared, and measurements \mathbf{e} are then produced for the sheared images to calculate the response for each object.

As discussed in §1, the detection of objects is shear-dependent. In particular, the number of objects detected depends on shear, and we wish to accurately account for this effect in the response. To address this we will repeat the detection on artificially sheared images, which will result in detection catalogs that differ for each sheared image. There is no single static catalog with which to generate postage stamps and make individual response measurements.

We can address this by moving the derivative outside of the average:

$$\begin{aligned} \langle \mathbf{R} \rangle &= \left. \frac{\partial \langle \mathbf{e} \rangle}{\partial \gamma} \right|_{\gamma=0}, \\ \langle R_{ij} \rangle &= \frac{\langle e_i^+ \rangle - \langle e_i^- \rangle}{\Delta \gamma_j} \end{aligned} \quad (5)$$

The finite difference is now calculated over averages, based on detections derived from the different sheared images. In general, only a subset of the detected objects will be common to all detection catalogs. Note that Equation 5 is entirely equivalent to the response Equation 14 of Sheldon & Huff (2017) in the case of a static catalog. We call this modified version of the method METADETECTION.

In what follows we will use simulations to test METACALIBRATION with and without including detection in the process. We will demonstrate that, for standard detection algorithms, including detection is required to obtain accurate shear estimates when galaxies are blended.

3. ANALYSIS AND SIMULATION TECHNIQUES

In this section, we describe our object simulation and measurement techniques. In all cases, we used the GALSIM (Rowe et al. 2015) software package to generate images, perform convolutions etc. We used the SEP (Barbary et al. 2017) Python wrapper of the SOURCE EXTRACTOR software package (Bertin & Arnouts 1996) for source detection as needed. Finally, we used the ngmix software package¹ for object measurement and the METACALIBRATION implementation.

3.1. Multi-object Fitting Deblending

Multi-object Fitting (MOF) deblending is a technique employed by the Dark Energy Survey to account for

¹ <https://github.com/esheldon/ngmix/>

blending of objects when performing image measurements (Drlica-Wagner et al. 2018). It is representative of a set of techniques that involve fitting models to images for a list of preexisting detections. The model fit is then used directly to form a flux measurement or indirectly by using it to approximately remove the light of the neighboring objects in the image before further processing.

In this work, we used an `ngmix` based MOF algorithm². It is an improved version of the MOF fitter used in Drlica-Wagner et al. (2018) which is both more stable and faster. It uses a linear combination of a De Vaucouleurs’ (de Vaucouleurs 1948) profile and exponential profile. The profiles are constrained to be cocentric, coelliptical, and to have a fixed one-to-one size ratio. The relative amplitude of the two profiles, the fraction of the total flux in the De Vaucouleurs’ profile, is a free parameter in the model. Finally, to process a large number of objects, we followed Drlica-Wagner et al. (2018) and broke them up into associated groups. These groups of objects were then simultaneously fit using a least-squares loss function. When using MOF with METACALIBRATION, we created postage stamp images centered on each object and subtracted the light of neighbors using the MOF models.

3.2. Galaxy Pair Simulations

In order to isolate the effects of detection, we employed a simulation setup consisting of two galaxies. By varying the separation between the two galaxies we could carefully tune the effects of blending.

The simulated galaxies were each a combination of a bulge component, modeled as a De Vaucouleurs’ profile (de Vaucouleurs 1948) and disk component modeled as an exponential. The fraction of light in the bulge was random and ranged uniformly between 0.0 and 1.0. The disk ellipticity was drawn from the distribution presented in Bernstein & Armstrong (2014), equation 24, with ellipticity variance set to 0.20, with a random orientation. The bulge was given the same orientation as the disk but with ellipticity set to the disk ellipticity times a random number drawn uniformly between 0.0 and 0.5. The half-light radius of the disk r_{50}^{disk} was set to a uniform random draw between 0.4 and 0.6 arcsec. The half-light radius of the bulge was a random draw between $0.4r_{50}^{\text{disk}}$ and $0.6r_{50}^{\text{disk}}$. The bulge was shifted from the center of the disk within a radius $0.05r_{50}^{\text{disk}}$ and in a random direction. The light of the disk was divided between a smooth component and a set of simulated “knots of star formation”, represented by point sources placed randomly with the same exponential distribution as the disk. Between 1 and 50 knots were placed, such that the fraction light in the knots ranged between 0.4% and 20%. The total flux and noise were set such that the signal-to-noise ratio ranged uniformly between 25 and 35. The models were convolved by a PSF modeled as a Moffat (Moffat 1969) profile with $\beta = 2.5$ and full width at half maximum 0.9 arcseconds, and rendered into an image with pixel scale 0.263 arcseconds.

We rendered two of these randomly generated galaxies in an image, with separation ranging from 1.0 and 4.0 arcsec. The pair was situated such that the line between the pair had a uniform random orientation relative to

the coordinate axes. Each object was given an additional random dither within a pixel. The galaxies were treated as transparent, such that the value in a pixel was equal to the total sum from both galaxies plus noise. Example images are shown in Figure 2

3.3. Simulations with Representative Galaxy Density and Noise

In this section we describe simulations with parameters chosen to mimic DES and LSST images. We used the publicly available `WeakLensingDeblending` software package (Kirkby, D. and Mendoza, I., and Sanchez, J. 2020; Sanchez, J., et al. 2021)³ to generate galaxy catalogs and images properties.

We generated images in the r-, i-, and z-bands with an effective depth that is roughly equivalent to full 5 and 10 year coadd image for the DES and LSST respectively. For our primary tests, we neglected the effects of PSF variation and used a constant PSF per-band with the typical (expected) seeing for each survey (~ 1 arcsec and ~ 0.8 arcsec respectively). We tested variable PSFs separately, as discussed in §6. For the DES image simulations, we modified the settings slightly such that the effective exposure time was equivalent to ten 90 second exposures. The depths of the LSST images were set to match those assumed by the `WeakLensingDeblending` package for the 10 year survey, although note the modifications below. In all simulations a shear of $\gamma_1 = 0.02$ was used.

We made two additional modifications to the simulations produced by this package. The galaxy models and PSFs were generated using the `WeakLensingDeblending` package, using its internal survey settings and object catalogs. But rather than using the package to render into an image, we rendered them separately so that we could control whether the full scene was sheared, including the space between objects, or just the objects were sheared (the only mode supported by `WeakLensingDeblending`).

We also multiplied the density of input sources by a factor of 0.45 and a factor of 0.4 for the DES-like and LSST-like simulations, respectively, in order to produce a realistic number density of detected sources. We also performed tests with the unmodified input catalog for the LSST-like simulations, in order to test with an extreme density. The detected source densities in these three simulations were approximately 35 per square arcmin for DES year 5, 75 per square arcmin for LSST year 10, and 140 per square arcmin with the unmodified source catalog for the LSST-like simulations. Example images for each survey are shown in Figure 3.

3.4. Measuring Shear Biases

We report our results in terms of the standard parameterization of shear measurement biases (see, e.g., Heymans et al. 2006)

$$g \equiv c + (1 + m)\gamma \quad (6)$$

where g is the recovered shear, c is the additive bias, and m is the multiplicative bias. Below we report only m , but we have found that c is consistent with zero in all cases.

² <https://github.com/esheldon/mof/>

³ <https://github.com/LSSTDESC/WeakLensingDeblending>

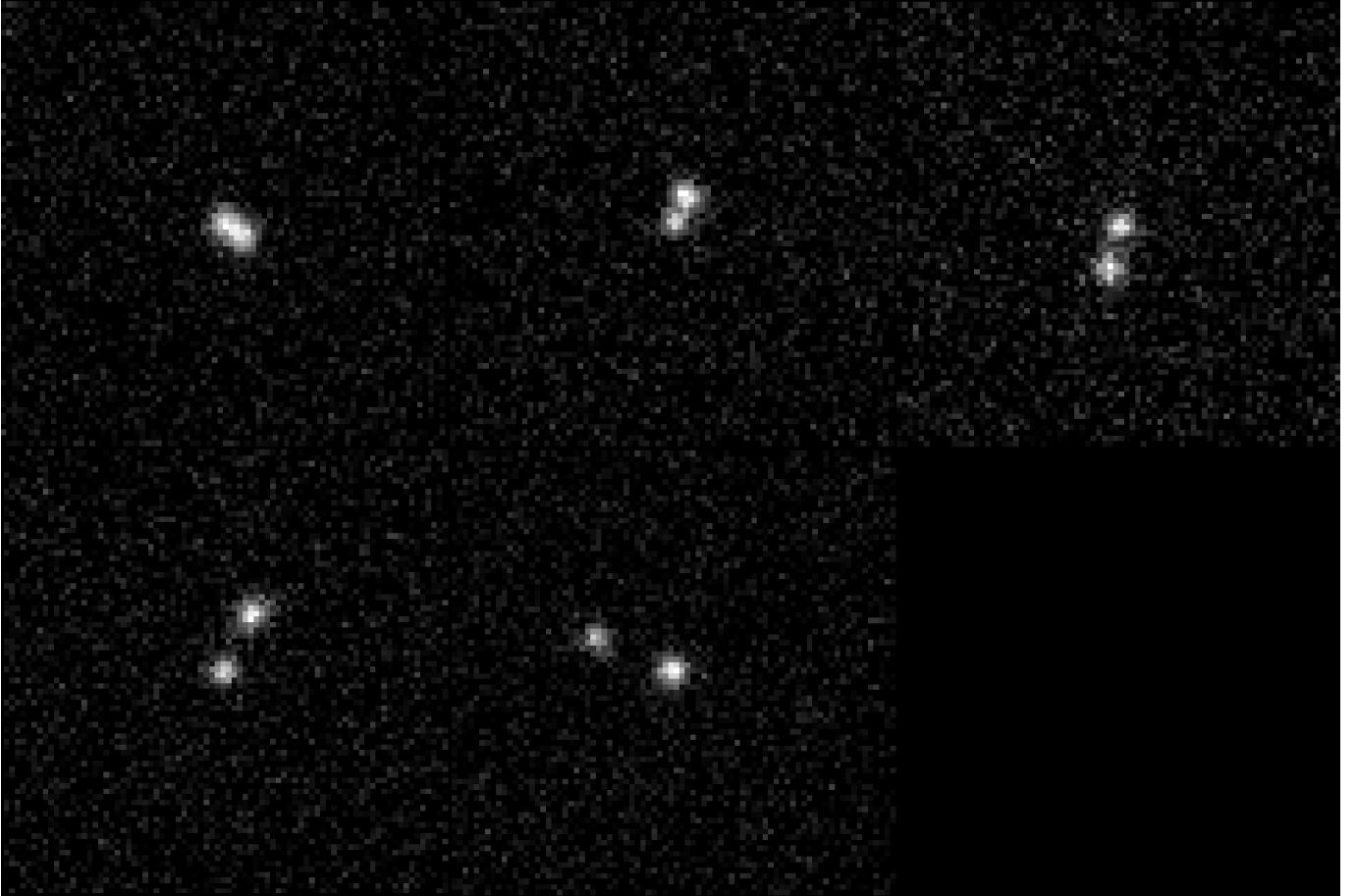


Figure 2. Example images of simulated galaxies used for the pair tests presented in section 3.2. From left to right in the top row, the separations are 1.0, 1.5, 2.0 arcsec. From left to right in the bottom row the separations are 3.0 and 4.0 arcsec. The pixel scale is 0.263 arcsec.

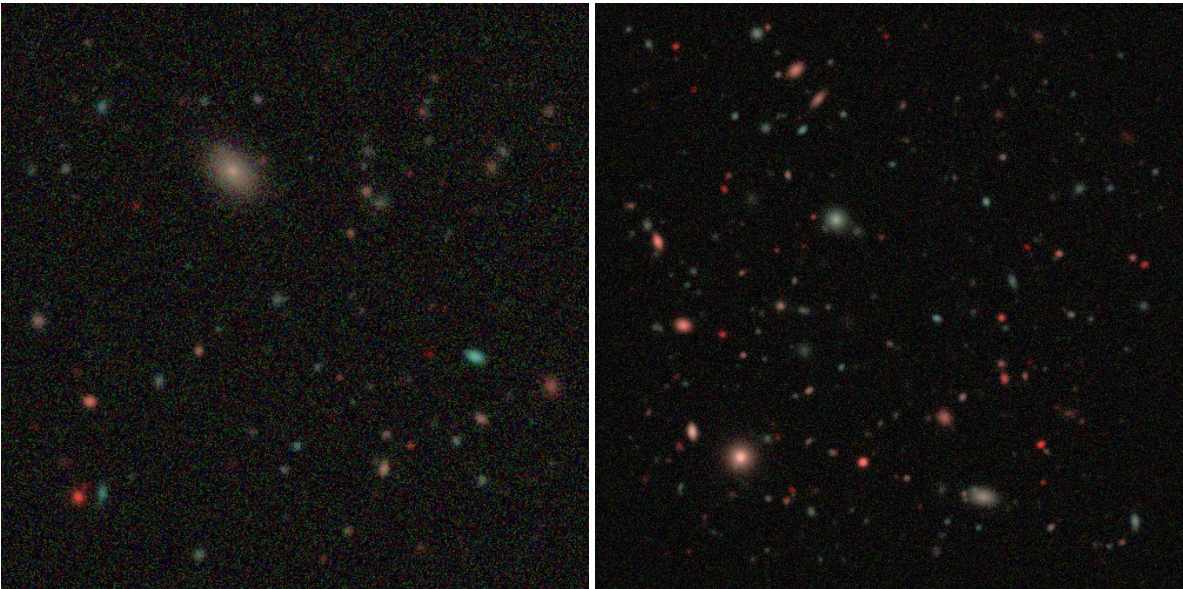


Figure 3. Example images from the DES (left) and LSST (right) simulations. Each multicolor, *gri*-band image is approximately ~ 2.2 arcmin on a side. The DES images have a pixel scale 0.263 arcsec and a PSF FWHM of ~ 1 arcsec. The LSST images have a pixel scale of 0.2 arcsec and a PSF FWHM of ~ 0.8 arcsec.

We used the technique of Pujol et al. (2019) to reduce the noise on measurements of m in our simulations. This technique works as follows. We generated pairs of images with identical galaxy and noise properties, but with opposite true shears applied γ_{\pm} (we use a scalar notation because the shear was only applied in one component). For each pair of simulations, we calculate the mean ellipticity and mean response. We then calculate ensemble means $\langle e_{\pm} \rangle$ and $\langle R \rangle = (\langle R_{+} \rangle + \langle R_{-} \rangle)/2$ over all such pairs of images, and form a difference of the overall recovered shear that partially cancels noise:

$$\gamma_{est} = \frac{\langle e_{+} \rangle - \langle e_{-} \rangle}{2\langle R \rangle}, \quad (7)$$

We then calculated m using equation 6, γ_{est} and the true input shear. We estimated the errors on the mean m using bootstrap resampling of the set of image pairs, repeating the computation of m for each bootstrap sample. We employed a similar procedure for c , except that we used the average of the two estimated shears so that any additive biases common to both simulations do not cancel. In all cases we measured m using the 1-component of the shear and c with the 2-component of the shear, though we have found this choice not to matter in explicit testing.

Note that, in the case that the entire scene is sheared, including the space between objects, the technique of Pujol et al. (2019) does not cancel the noise as effectively as when only the shapes of objects are sheared. This is because the objects move differently under the two different shears and thus sample slightly different parts of the noise field.

4. SHEAR-DEPENDENT DETECTION BIASES

In this section, we present results from a set of experiments using image simulations designed to elucidate the role of detection biases in METACALIBRATION shear measurements. We first examine shear measurement on pairs of galaxies at various separations. We then study detection biases in DES- and LSST-like simulations with realistic galaxy densities and pixel noise. We find in all cases that object detection imparts a significant shear measurement bias. As we will show in §5.1, we can correct this bias by including detection in the METACALIBRATION process, even if no explicit deblending (division of light between objects) is performed.

4.1. Basic Analysis Method

The full METADETECTION analysis method, which includes detection in the METACALIBRATION process, was outlined in §1 and the formalism for calibration was given in §2. In the sections §4.2 and §4.3 that follow, we show shear recovery bias using standard METACALIBRATION, without the full METADETECTION. Rather than shearing a large image and repeating detection, we ran detection once to produce a static detection catalog. We then performed basic METACALIBRATION on postage stamps for each detection. During the measurement phase, we performed deblending using the MOF algorithm described in §3.1. We also ran tests without deblending, using simple weighted moments, and saw biases at a similar level, but do not show the results for the sake of brevity.

4.2. Bias in Simulations of Galaxy Pairs

We tested METACALIBRATION with using the galaxy pair simulation presented in §3.2. We used SOURCE EXTRACTOR for object detection, with settings matching those used for DES year 5 survey reductions (DES Collaboration, in prep.)⁴. We got similar results using a simple local peak finder for detection⁵. We also saw similar levels of bias with and without performing deblending using MOF.

The multiplicative bias m is shown in Figure 4 as a function of the pair distance. For a large separation of 4 arcsec, two objects were detected in essentially all cases, but as the separation was decreased the detection became more ambiguous, with only one object detected in some cases. At 1.5 arcsec separation the detection was most ambiguous, with two objects detected in half the cases. As the separation was decreased further, one object was detected more often than two, and at 1.0 arcseconds only one object was detected in essentially all cases. For close separations the blend is unrecognized but the detection is unambiguous, in the sense that the detection algorithm consistently finds one object.

In the cases where the detection is unambiguous, at close and far separations, there is no bias in the recovered shear. But the bias increases as the detection becomes more ambiguous. The maximum bias occurs at 1.5 arcsec separation, where two objects are detected in half the cases, the separation of maximum ambiguity.

The correspondence between detection ambiguity and shear bias is a hint that the bias is caused by shear-dependent detection. Next, we test with simulations of DES- and LSST-like surveys and show explicitly that by making object detection shear independent, we can eliminate these detection biases.

4.3. Bias in Simulations with Representative Galaxy Density and Noise

The results for simulations with representative galaxy density and noise are shown in Table 1. METACALIBRATION with MOF deblending and SOURCE EXTRACTOR detections results in large biases, $\sim -3\%$, for a full five year DES-like survey. Simulations of LSST-like surveys demonstrate somewhat larger biases, and a simulation with double the LSST galaxy density shows a very large bias. Note, we see similar biases when no deblending is performed but we again omitted them from the table for the sake of brevity.

The bias numbers presented above are relatively noisy, but it is interesting to note that the bias for LSST year 10 is not very much larger than DES year 5, despite the fact that the galaxy density is about twice as high. This may be partly due to the better resolution of the LSST images: the area of the LSST PSF is 60% smaller than DES PSF. Thus the images of small galaxies, at fixed density, will overlap less in LSST images than they do in DES images.

In order to unpack the source of the bias in this case, we compared two different METACALIBRATION shear measurements. The first was performed on a catalog of the

⁴ We have created a software package to run detection with DES year 5 settings, using the sep SOURCE EXTRACTOR wrapper <https://github.com/esheldon/sxdes>

⁵ <https://github.com/esheldon/peaks>

Table 1

Multiplicative biases in weak lensing simulations for various shear measurement techniques. In all cases, the simulations use realistic galaxy ellipticities, galaxy sizes and noise for the given survey. For measurements using standard METACALIBRATION with MOF deblending, a cut of $T/T_{PSF} > 0.5$ was also applied. Measurements with METADETECTION and moments used a size cut of $T/T_{PSF} > 1.2$. In the case of METADETECTION with moments, no deblending corrections are applied and the moments are a simple weighted moment with no PSF correction.

Simulation	Method	Full Scene Sheared?	S/N Cut	m
metacal+MOF - full scene sheared				
DESY5	metacal+MOF	yes	$S/N > 10$	-0.036 ± 0.005
DESY5	metacal+MOF	yes	$S/N > 15$	-0.023 ± 0.004
DESY5	metacal+MOF	yes	$S/N > 20$	-0.015 ± 0.004
LSSTY10	metacal+MOF	yes	$S/N > 10$	-0.035 ± 0.002
LSSTY10	metacal+MOF	yes	$S/N > 15$	-0.031 ± 0.002
LSSTY10	metacal+MOF	yes	$S/N > 20$	-0.026 ± 0.002
LSSTY10 2× dens.	metacal+MOF	yes	$S/N > 10$	-0.082 ± 0.005
LSSTY10 2× dens.	metacal+MOF	yes	$S/N > 15$	-0.067 ± 0.005
LSSTY10 2× dens.	metacal+MOF	yes	$S/N > 20$	-0.062 ± 0.004
metadetect+moments - full scene sheared				
DESY5	metadetect+moments	yes	$S/N > 10$	$+0.00025 \pm 0.00088$
DESY5	metadetect+moments	yes	$S/N > 15$	-0.00085 ± 0.00070
DESY5	metadetect+moments	yes	$S/N > 20$	$+0.00024 \pm 0.00061$
LSSTY10	metadetect+moments	yes	$S/N > 10$	$+0.00084 \pm 0.00061$
LSSTY10	metadetect+moments	yes	$S/N > 15$	-0.00001 ± 0.00047
LSSTY10	metadetect+moments	yes	$S/N > 20$	$+0.00042 \pm 0.00039$
LSSTY10 2× dens.	metadetect+moments	yes	$S/N > 10$	$+0.00047 \pm 0.00043$
LSSTY10 2× dens.	metadetect+moments	yes	$S/N > 15$	-0.00002 ± 0.00034
LSSTY10 2× dens.	metadetect+moments	yes	$S/N > 20$	$+0.00019 \pm 0.00028$
metadetect+moments - individual objects sheared				
DESY5	metadetect+moments	no	$S/N > 10$	-0.0042 ± 0.0009
DESY5	metadetect+moments	no	$S/N > 15$	-0.0052 ± 0.0006
DESY5	metadetect+moments	no	$S/N > 20$	-0.0059 ± 0.0006
DESY5 2× dens.	metadetect+moments	no	$S/N > 10$	-0.0029 ± 0.0006
DESY5 2× dens.	metadetect+moments	no	$S/N > 15$	-0.0017 ± 0.0005
DESY5 2× dens.	metadetect+moments	no	$S/N > 20$	-0.0023 ± 0.0005
LSSTY10	metadetect+moments	no	$S/N > 10$	-0.0015 ± 0.0007
LSSTY10	metadetect+moments	no	$S/N > 15$	-0.0013 ± 0.0006
LSSTY10	metadetect+moments	no	$S/N > 20$	$+0.0001 \pm 0.0005$
LSSTY10 2× dens.	metadetect+moments	no	$S/N > 10$	-0.0047 ± 0.0006
LSSTY10 2× dens.	metadetect+moments	no	$S/N > 15$	-0.0035 ± 0.0004
LSSTY10 2× dens.	metadetect+moments	no	$S/N > 20$	-0.0029 ± 0.0004

true source positions using a fixed 1.2 arcsecond Gaussian weighted moment ellipticity measurement. We did not run MOF deblending on the true detection catalog. The true catalog is very dense, which means the blended groups would be very numerous and would have many members. Because there is a large computing overhead associated with the deblending, the running time would have been prohibitively slow.

The second measurement employed METACALIBRATION with the same weighted moment ellipticity measurement, but using SOURCE EXTRACTOR detections rather than the true object positions.

We found that, while the METACALIBRATION shear measurement using true detections is unbiased (-0.0011 ± 0.0012), the measurement using SOURCE EXTRACTOR detections exhibits a bias of

-0.058 ± 0.001 . Note that this ellipticity measurement makes no corrections for object blending, but in the case where we use the true object positions, it is still unbiased. Thus we have demonstrated that, given a set of true source locations, METACALIBRATION is unbiased when objects are blended.

This set of tests also demonstrates explicitly that source detection can cause significant shear measurement biases even for techniques which are robust to blending. The source detection biases probably originate from multiple causes, but one of those causes is certainly the merging or splitting of object detections in a way that is shear dependent, as illustrated with the toy example in Figure 1 and the galaxy pair tests above.

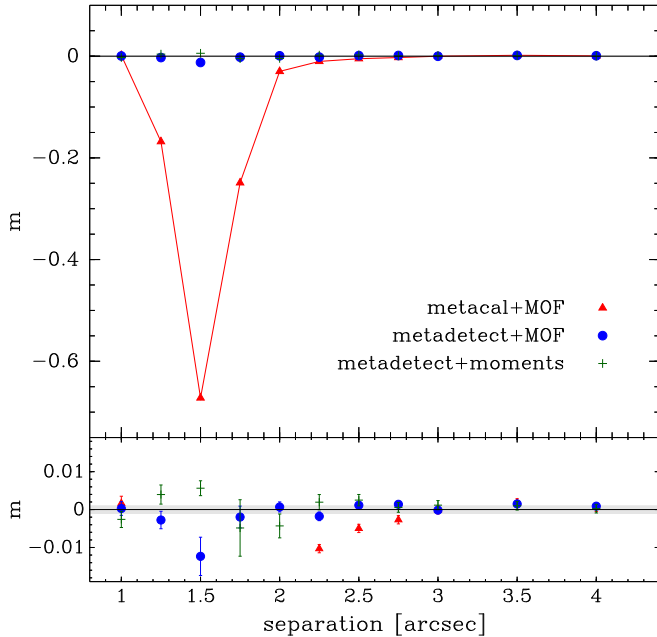


Figure 4. Mean multiplicative shear bias measured for pairs of simulated galaxies (see §3.2 for details) at various separations. At each separation, a large number of trials was generated with random orientations of the pair. At 4.0 arcsec separation, two objects were detected in all cases. At 1.5 arcseconds two objects were detected in half the cases. At 1.0 arcsec a single object was detected in all cases. Red triangles represent standard METACALIBRATION with MOF deblending for modeling all detected objects. Blue circles represent METACALIBRATION+MOF with detection included as part of the process. Green pluses represent METACALIBRATION with detection included but without deblending, and using simple weighted moments without PSF correction as the shear estimator. Very large biases are seen for standard METACALIBRATION+MOF as detection becomes ambiguous, for example at 1.5 arcsec separations. When detection is included in the METACALIBRATION process the biases are greatly reduced. The bias is reduced even in the case where no deblending was performed and no PSF correction or detailed object modeling were performed. This indicates that a majority of the bias is due to shear-dependent detection, not light blending or details of the object modeling.

5. MITIGATING SHEAR-DEPENDENT DETECTION BIASES

In the previous section, we demonstrated that source detection is a significant source of bias in shear measurements with METACALIBRATION. Here we show we can mitigate this bias by including source detection in the METACALIBRATION process. For these tests, we use the full METADETECTION algorithm outlined in §1, which involves first producing large sheared versions of the image, followed by running detection separately on each sheared image.

We performed object detection on each image using SOURCE EXTRACTOR. We then made measurements in postage stamps around each detection in each image using a non-PSF corrected, Gaussian-weighted moment. We used these five catalogs to calculate a single estimate for the shear using the mean shear response for the image as shown in 5 from §2, which we repeat here for clarity:

$$\langle \gamma \rangle \approx \langle \mathbf{R} \rangle^{-1} \langle \mathbf{e} \rangle$$

$$\langle R_{ij} \rangle = \frac{\langle e_i^+ \rangle - \langle e_i^- \rangle}{\Delta \gamma_j}. \quad (8)$$

We here reiterate that the averages above are over measurements from different *detection catalogs*, generated by running source detection and ellipticity measurement on differently sheared images. Shear responses for individual detected objects, as used in both Sheldon & Huff (2017) and Huff & Mandelbaum (2017), were not calculated. Doing so would require matching the lists of detections found on the different sheared images, so that finite differences for each object could be formed. This act of matching would introduce the very shear-dependent object detection biases we wish to calibrate. We will discuss the implications of this fact for the analysis of imaging surveys in §7.

5.1. METADETECTION Results for Simulated Galaxy Pairs

In Figure 4 we show results for the simulations of galaxy pairs, now including detection in the METACALIBRATION process. The blue filled circles represent the case where deblending is performed using MOF. The green plus signs represent the case where no deblending was performed. For the case without deblending, we further simplified the process: we calculated simple weighted moments at the position determined by SOURCE EXTRACTOR using a fixed weight function with full-width at half maximum 1.2 arcsec, without any correction for the PSF.

In both cases the bias is greatly reduced, with significant bias seen only at the special separation of 1.5 arcsec, where the two objects are detected as one object by SOURCE EXTRACTOR in half of the cases. This demonstrates that the bias we see is not primarily due to the process of deblending itself, but rather shear-dependent detection effects. The remaining biases at 1.5 arcsec tend to be different sign for the deblended and non-deblended cases, which shows there is a qualitative difference in how the two measurements respond to the shear. As we will show below, we find no significant net bias for more realistic DES and LSST-like images where the typical separation of galaxies is not at a special value of maximum detection ambiguity.

5.2. METADETECTION Results for Simulations with Representative Galaxy Density and Noise

We show results for DES-like and LSST-like surveys in Table 1. We have used a constant PSF and constant shear for these simulations. Note we here only included METADETECTION with Gaussian weighted moment ellipticities, primarily to reduce the total CPU time used for the tests.

We find that in all cases our METADETECTION shear measurements are unbiased up to second-order shear effects (we expect a bias of a few parts in 10000 for shears of 0.02, see Sheldon & Huff 2017). This conclusion holds despite the extensive blending of the object images and the large source detection effects we documented above. They also meet or exceed the requirements for analyzing an LSST-like survey (e.g., Huterer et al. 2006). Finally, note that we have also shown results for an LSST-like survey where the number density of objects is approximately twice that expected from the actual survey. Even at these higher densities we find no increase in the shear bias.

5.3. Testing the Physical Assumptions Behind METADETECTION

Here we address a key physical assumption made by METADETECTION, namely that the space between all objects is sheared coherently. With METADETECTION we shear the entire image, so the space between objects is sheared as well as their shapes, and this is completely coherent across the image. In §5.2 we showed that, when the shear in the simulation matches this procedure exactly, we calculate the response accurately.

Real data, however, typically contains images of objects sheared by different amounts at different redshifts, and can be thought of as a sum of a series of constant, but differently sheared images. In such an image, the shearing is not completely coherent. Variable shear itself is not a source of bias for METADETECTION; the formalism presented in (Sheldon & Huff 2017) recovers the mean shear or other ensemble statistic for a population. But because the shearing of the space between objects in real data is not completely coherent, we may expect that the part of the METADETECTION response associated with detection is slightly biased.

In Figure 5 we show a toy example, similar to Figure 1, demonstrating the extreme and unphysical case of two objects that are in line-of-sight projection but sheared completely independently. We did not allow the space between objects to be sheared. The contours of constant surface brightness differ less after shear than those shown in 1. We find this intuitive, because the relative separation between objects does not change. The METADETECTION process of shearing the full image, which does move the positions of objects, will over-predict the response in this case.

In general, we expect a larger bias due to this effect for surveys with more object blending, which scales with object density and PSF size. In order to obtain an upper bound on this effect for real surveys, we made a simple modification to our simulations with realistic galaxy density and noise. When building them, rather than shearing the full scene to impart the true shear to the image, we sheared each object individually and then added it to the image, without any change in the object position. This modification leaves the space between objects un-sheared, which is maximally different from what happens during the METACALIBRATION image shearing process.

Results are shown in the bottom rows of Table 1. We found small residual biases in this case, of order $\sim -0.3\%$. The fact that we find more bias for a DES-like survey than an LSST-like survey might be explained by the large PSFs in the DES-like survey and the smaller pixel scale in the LSST-like survey. However, some of the DES-like results are puzzling. In particular, the trend with object density in the DES-like surveys appears to be opposite our naive expectation. We do not fully understand this effect. While predicting the expected level of this bias for experiments such as such as DES and LSST is essential, it is beyond the scope of this work.

6. HANDLING PSF VARIATION

In order to apply METADETECTION to a real, multi-band, multi-epoch survey like the DES or LSST, we must address realistic levels of PSF variation, missing data, and non-trivial WCS transformations. We will address

missing data and WCS issues in a future work, currently in preparation. Here we address the issue of PSF variation, which is technically the most challenging because METADETECTION requires deconvolution by the PSF over relatively large regions of sky.

The deconvolution of a spatially varying PSF formally requires a spatially varying kernel, the implementation of which would be computationally challenging. We instead adopted efficient FFTs for deconvolution, which require a constant kernel. For this kernel, we chose to use the PSF associated with the center of the final coadd image, which is thus systematically wrong at other locations and will necessarily produce a bias in the recovered shear. However, we will show that the image coadding process used in a realistic multi-epoch survey results in a more uniform PSF in the final coadd, and sufficiently reduces associated biases.

For these simulations, we used a simple population of galaxies that have exponential profiles with a half light radius of 0.5 arcsec. All of the objects were round and were rendered at a signal-to-noise ratio greater than 20. These simulations had very low ellipticity noise and so could reach a high precision with a relatively small number of images. We created the images for the simulation by coadding a number of images with random, variable PSFs. METADETECTION was then performed using the coadd of PSF models from the input images, with the PSF from each input image generated at the location of the center of the final coadd.

In order to place an upper bound on this effect, we created a variable PSF model that had significantly more variation than we expect in real data. See Appendix A for details. Using a single PSF realization from Appendix A, without coadding, we found a multiplicative bias of -0.0065 ± 0.00044 . However, when coadding thirty of these models, which is the expected number of epochs for three bands in the final DES data set, we found a multiplicative bias of only -0.00035 ± 0.00037 . For LSST many more epochs will be available for coadding. While this test is not conclusive, we expect that in a realistic survey scenario, PSF variation will not be a fundamental limitation for METADETECTION.

7. IMPLICATIONS FOR THE ANALYSIS OF IMAGING SURVEYS

The fact that five separate catalogs must be used without any attempt at matching them (see §5), has implications for using METADETECTION in the analysis of surveys. Typically a single reference or “gold” sample of objects is constructed and used for all subsequent calculations, such as calculating redshift distributions. With METADETECTION, multiple such catalogs, one for each artificial shear, must be constructed in order to understand the response of summary statistics to shear. Specifically, the process of selecting objects, such as removing objects with low signal-to-noise ratio or sorting objects into redshift bins, must be repeated using the measurements made on sheared images in order to include selection effects (Sheldon & Huff 2017).

When calculating sums and averages for other, non-shear quantities, such as a redshift distribution, the appropriate object-by-object weight is the shear response (Sheldon & Huff 2017). But individual responses can-

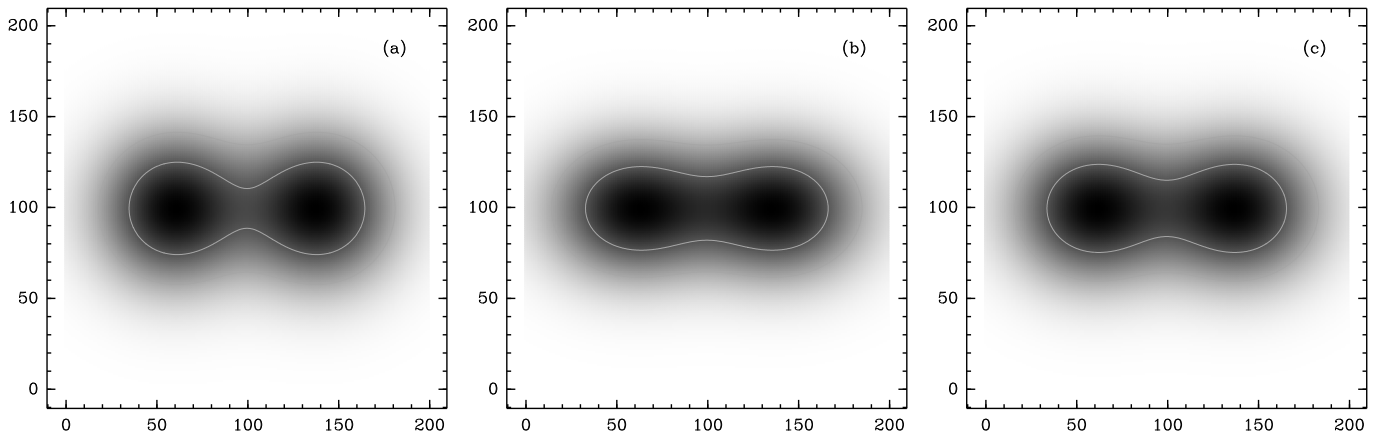


Figure 5. Same as Figure 1 but the shear was applied to the objects without shearing the space between them. This models the extreme and unphysical case where two objects are in line-of-sight projection but sheared completely independently. The contours changed less after shearing in this case as compared to the contours in Figure 1. This case differs from the METADETECTION process, in which the entire image is sheared, including the space between images.

not be calculated with METADETECTION, because this would require matching the catalogs produced from the different artificially sheared images, which would introduce shear-dependent selection effects. It may be possible to derive an appropriate mean weight using ensemble statistics. For example, one could define fine redshift bins (different from the bins used for tomography) and calculate the mean response in those bins using the separate sheared versions of the catalogs. This could then be interpolated to provide weights for objects when constructing the redshift distribution in tomographic bins. We will study this issue in more detail in a future work.

8. SUMMARY

In this work, we explored how METACALIBRATION weak lensing measurements perform in scenarios where the images of objects overlap and the detection of objects can be ambiguous. These conditions will characterize all future weak lensing surveys, especially those executed beneath the atmosphere where PSF smearing significantly increases the blending of images, so accurate performance in this regime is critical. We showed that METACALIBRATION has many percent biases that get worse as the degree of blending increases, even when objects are deblended. We then demonstrated that we can accurately eliminate these biases by including the detection of objects in the METACALIBRATION process, even for an LSST-like survey. We call this technique METADETECTION.

We tested an important assumption of METADETECTION, that the space between objects in an image is sheared coherently, an assumption that does not perfectly match real data. We placed an upper bound on the bias associated with this effect at a few tenths of percents for future surveys. More detailed study will be needed to predict the actual effect for specific data sets.

In future work we must address a number of technical challenges associated with implementing METADETECTION on real data. We must run METADETECTION over relatively large images ($\sim 1 - 2$ arcminutes on a side) in order efficiently capture ambiguities in the detection of objects. Detection is less efficient in smaller images, because the larger perimeter to area ratio re-

sults in a higher fraction of objects, including blends, near the edge. Also, over these large scales, the assumption that the PSF and world coordinate system (WCS) transformations are approximately constant is incorrect, complicating the application of an artificial shear. We have shown in this work that PSF variation is unlikely to be a problem when coadding many tens of images. However, in order to reconstruct accurate PSF models for the coadd, the input images can have no edges within the coadd region. This requirement means some images must be left out of the coadd process, resulting in some loss of some precision (Armstrong, R., et al. 2020). Finally, we should be able to handle non-constant WCS transformations by coadding the images into a nearly constant WCS, but this procedure remains to be tested.

Additional issues arise from masking. Large regions of images can have non-trivial masking patterns due to stellar diffraction spikes, streaks from moving objects, cosmic rays, etc. In the implementation presented in this work, we use fast Fourier transforms (FFTs) to handle convolutions. The FFT does not permit missing data, so the masked regions must be interpolated in some way. Care must be taken that this interpolation does not introduce a spurious shear signal. An additional compensating mask, rotated at right angles to the real mask, can be used to restore symmetry to the image (Sheldon & Huff 2017). The camera rotations planned for the Rubin telescope will accomplish this cancellation of systematic effects even more efficiently. Also, interpolation correlates the noise in the image, as does the coadding process itself, so the noise field used for correcting correlated noise effects must also be propagated through the same coadding and interpolation (Sheldon & Huff 2017; Armstrong, R., et al. 2020).

Finally, the five separate METADETECTION catalogs must each be incorporated into the full set of downstream analysis tasks (e.g., photometric redshift estimation, the construction of summary statistics, etc.) in order to be used for cosmological constraints (see §7 for details). This should be straightforward, but it does require a small change to how shear data are analyzed.

The degree to which these technical challenges can be overcome will ultimately determine the accuracy of

METADETECTION when used to analyze imaging survey data.

ACKNOWLEDGMENTS

ES is supported by DOE grant DE-AC02-98CH10886, and MB is supported by DOE grant DE-AC02-06CH11357. We gratefully acknowledge the computing resources provided on Bebop, a high-performance computing cluster operated by the Laboratory Computing Resource Center at Argonne National Laboratory, and the RHIC Atlas Computing Facility, operated by Brookhaven National Laboratory. This work also used resources made available on the Phoenix cluster, a joint data-intensive computing project between the High Energy Physics Division and the Computing, Environment, and Life Sciences (CELS) Directorate at Argonne National Laboratory.

REFERENCES

Armstrong, R., et al. 2020, in prep [8](#)
 Barbary, K., Boone, K., Craig, M., Deil, C., & Rose, B. 2017, kbarbary/sep: v1.0.2, doi: [10.5281/zenodo.896928](#) [3](#)
 Bernstein, G. M., & Armstrong, R. 2014, MNRAS, 438, 1880, doi: [10.1093/mnras/stt2326](#) [3.2](#)
 Bernstein, G. M., Armstrong, R., Krawiec, C., & March, M. C. 2016, MNRAS, 459, 4467, doi: [10.1093/mnras/stw879](#) [1](#)
 Bertin, E., & Arnouts, S. 1996, A&AS, 117, 393 [1](#), [3](#)
 Bosch, J., Armstrong, R., Bickerton, S., et al. 2018a, PASJ, 70, S5, doi: [10.1093/pasj/psx080](#) [1](#)
 Bosch, J., AlSayyad, Y., Armstrong, R., et al. 2018b, arXiv:1812.03248. <https://arxiv.org/abs/1812.03248> [1](#)
 Dawson, W. A., Schneider, M. D., Tyson, J. A., & Jee, M. J. 2016, ApJ, 816, 11, doi: [10.3847/0004-637X/816/1/11](#) [1](#)
 de Vaucouleurs, G. 1948, Annales d’Astrophysique, 11, 247 [3.1](#), [3.2](#)

APPENDIX

A. FAST APPROXIMATE VARIABLE PSF MODELS

In this work we used a fast, approximate variable PSF model. This model eases the computational requirements for the simulations while also retaining the essential features of realistic PSF variation. In this appendix, we present the model and verify its statistical properties against more realistic PSF models.

We began with the results of [Heymans et al. \(2012\)](#). They fit the von Kármán model of atmospheric turbulence

$$P(\ell) \propto \left(\ell^2 + \frac{1}{\theta_0^2} \right)^{-11/6}$$

to images with high stellar density. Here θ_0 is the outer scale of turbulence. ([Heymans et al. 2012](#)) find that $\theta_0 \approx 3$ arcmin. We further added an additional Gaussian truncation of the power

$$P_{trunc}(\ell) \propto P(\ell) \exp(-\ell^2 r^2)$$

at a scale of $r = 1$ arcsec in order to reduce the level of resulting PSF variation. Below we show that even with this modification, our models still have more power than a realistic model for a survey, making them useful for providing upper limits on the effects of PSF variation.

Using this model, we seeded equal amounts of E- and B-mode power on a grid of 128×128 cells using random phases. Each cell of the grid was one arcsec in size. We

Drlica-Wagner, A., Sevilla-Noarbe, I., Rykoff, E. S., et al. 2018, ApJS, 235, 33, doi: [10.3847/1538-4365/aab4f5](#) [3.1](#)
 Fenech Conti, I., Herbonnet, R., Hoekstra, H., et al. 2017, MNRAS, 467, 1627, doi: [10.1093/mnras/stx200](#) [1](#)
 Heymans, C., Kitching, T., Rowe, B., et al. 2012, Monthly Notices of the Royal Astronomical Society, 421, 381, doi: [10.1111/j.1365-2966.2011.20312.x](#) [A](#)
 Heymans, C., Van Waerbeke, L., Bacon, D., et al. 2006, MNRAS, 368, 1323, doi: [10.1111/j.1365-2966.2006.10198.x](#) [3.4](#)
 Huff, E., & Mandelbaum, R. 2017, arXiv:1702.02600. <https://arxiv.org/abs/1702.02600> [1](#), [1](#), [5](#)
 Huterer, D., Takada, M., Bernstein, G., & Jain, B. 2006, MNRAS, 366, 101, doi: [10.1111/j.1365-2966.2005.09782.x](#) [1](#), [5.2](#)
 Jee, M. J., & Tyson, J. A. 2011, PASP, 123, 596, doi: [10.1086/660137](#) [A](#), [A2](#)
 Kirkby, D. and Mendoza, I., and Sanchez, J. 2020, WeakLensingDeblending, 1.0.0, Zenodo, doi: [10.5281/zenodo.3975230](#) [3.3](#)
 Li, X., Katayama, N., Oguri, M., & More, S. 2018, MNRAS, 481, 4445, doi: [10.1093/mnras/sty2548](#) [1](#)
 Mandelbaum, R., Rowe, B., Bosch, J., et al. 2014, ApJS, 212, 5, doi: [10.1088/0067-0049/212/1/5](#) [A](#)
 Mandelbaum, R., Miyatake, H., Hamana, T., et al. 2018, PASJ, 70, S25, doi: [10.1093/pasj/psx130](#) [1](#)
 Moffat, A. F. J. 1969, A&A, 3, 455 [3.2](#)
 Pujol, A., Kilbinger, M., Sureau, F., & Bobin, J. 2019, A&A, 621, A2, doi: [10.1051/0004-6361/201833740](#) [3.4](#), [3.4](#)
 Rowe, B. T. P., Jarvis, M., Mandelbaum, R., et al. 2015, Astronomy and Computing, 10, 121, doi: [10.1016/j.ascom.2015.02.002](#) [3](#)
 Sanchez, J., et al. 2021, in prep, doi: [10.5281/zenodo.3975230](#) [3.3](#)
 Schneider, P., Ehlers, J., & Falco, E. E. 1992, Gravitational Lenses (Gravitational Lenses, XIV, 560 pp. 112 figs., Springer-Verlag Berlin Heidelberg New York. Also Astronomy and Astrophysics Library) [1](#)
 Sheldon, E. S., & Huff, E. M. 2017, ApJ, 841, 24, doi: [10.3847/1538-4357/aa704b](#) [1](#), [1](#), [1](#), [2](#), [5](#), [5.2](#), [5.3](#), [7](#), [8](#)
 Zuntz, J., Sheldon, E., Samuroff, S., et al. 2018, MNRAS, 481, 1149, doi: [10.1093/mnras/sty2219](#) [A](#)

normalized the overall ellipticity variance to 0.10^2 . We then used the g_1 and g_2 components of this model to set the variation of the ellipticity of the PSF. We drew the mean ellipticity for each image from a Gaussian distribution of variance 0.10^2 . Note that we also bound the total ellipticity to at most 0.5. We modeled the PSF profile as a Moffat with shape parameter $\beta = 2.5$. The size of the Moffat profile was set to be proportional to $\mu^{-3/4}$, where μ is the magnification computed from the power spectra realization. The proportionality constant was drawn randomly from a log-normal model with scatter 0.1 arcmin and a central value set so the final PSF size mimicked a DES-like survey, with focal plane averaged FWHM ~ 1.1 arcsec.

We show an example PSF for a DES-like survey in [Figure A1](#). Over a 1 square arcminute patch, our approximate models generate PSF ellipticity and size variation that are $\gtrsim 10\times$ that seen in real 90 second exposures with DECam ([Zuntz et al. 2018](#)), or the expected variation in a 15 second exposure with LSST ([Jee & Tyson 2011](#)) over similar scales. [Figure A2](#) shows the ξ_{\pm} shear correlation functions averaged over 100 realizations of our models. For comparison, we expect at most shear correlation function amplitudes of $\sim 10^{-4}$ for LSST ([Jee & Tyson 2011](#)) and for DECam 90 second exposures. The DECam models were generated using the methods of [Jee & Tyson \(2011\)](#) but for DECam-like environmental conditions. For the optical contributions to the PSF, we use a set of randomly drawn aberrations (similar to GREAT3 ([Mandelbaum et al. 2014](#))), but with values more typical

of DECam observations⁶.

⁶ <https://github.com/GalSim-developers/GalSim/blob/master/releases/2.1/examples/great3/cgc.yaml>

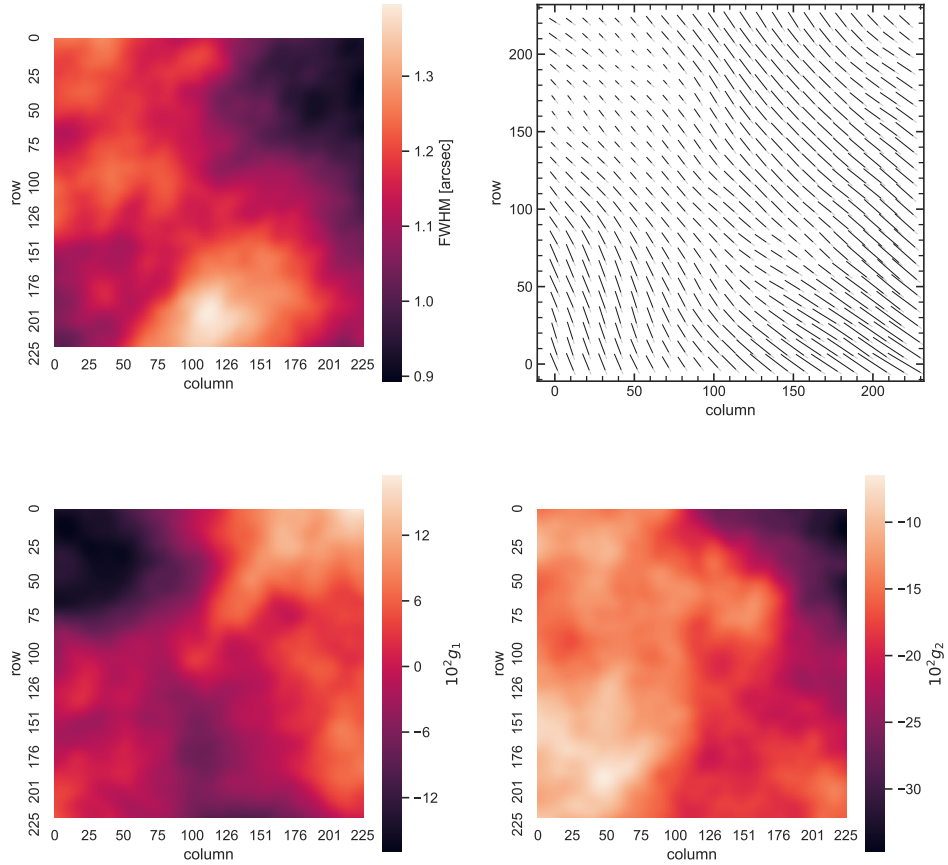


Figure A1. Variable PSF model statistics for a DECam-like exposure. The top-left panel shows the variation in the FWHM in arcseconds. The top-right panel shows a visualization of the PSF ellipticity variation. The bottom-left panel shows the variation in the 1-component of the PSF ellipticity. The bottom-right panel shows the variation in the 2-component of the PSF ellipticity. The variation in this model is $\gtrsim 10\times$ larger than the typical PSF variation for either DECam or expected LSST observations. The pixel scale is 0.263 arcsec so that each panel is approximately 1 arcmin on a side.

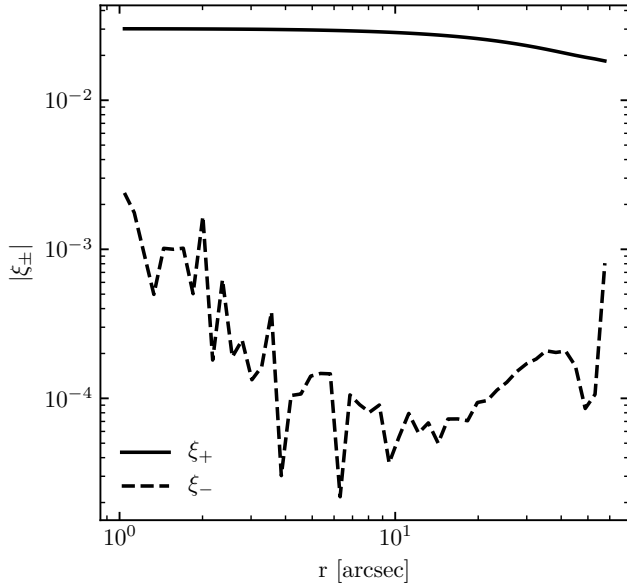


Figure A2. Variable PSF model shear correlation functions for a DECam-like exposure. LSST is expected to have shear correlation function magnitudes around $\sim 10^{-4}$ (Jee & Tyson 2011).